

Molecular-hybridization-induced antidamping and sizeable enhanced spin-to-charge conversion in $\text{Co}_{20}\text{Fe}_{60}\text{B}_{20}/\beta\text{-W/C}_{60}$ heterostructures

Antarjami Sahoo^{ID, 1}, Aritra Mukhopadhyaya^{ID, 2}, Swayang Priya Mahanta^{ID, 1}, Md. Ehesan Ali^{ID, 2,*}, and Subhankar Bedanta^{ID, 1,3,†}

¹*Laboratory for Nanomagnetism and Magnetic Materials (LNMM), School of Physical Sciences, National Institute of Science Education and Research (NISER), An OCC of Homi Bhabha National Institute (HBNI), Jatni, Odisha 752050, India*

²*Institute of Nano Science and Technology, Knowledge City, Sector-81, Mohali, Punjab 140306, India*

³*Center for Interdisciplinary Sciences (CIS), National Institute of Science Education and Research (NISER), An OCC of Homi Bhabha National Institute (HBNI), Jatni, Odisha 752050, India*

(Received 27 October 2023; revised 23 February 2024; accepted 5 April 2024; published 1 May 2024)

The development of power-efficient spintronic devices has been a compelling need in the post-CMOS technology era. The effective tuneability of spin-orbit coupling (SOC) in the bulk and at the interfaces of hybrid material stacks is a prerequisite for scaling down the dimensions and power consumption of these devices. In this work, we demonstrate the strong chemisorption of C_{60} (fullerene) molecules when grown on the high-SOC $\beta\text{-W}$ layer. The parent $\text{Co}_{20}\text{Fe}_{60}\text{B}_{20}/\beta\text{-W}$ (CFB/ $\beta\text{-W}$) bilayer exhibits large spin-to-charge interconversion efficiency, which can be ascribed to the interfacial SOC observed at the ferromagnet/heavy-metal interface. Further, the adsorption of C_{60} molecules on $\beta\text{-W}$ reduces the effective Gilbert damping by $\sim 15\%$ in CFB/ $\beta\text{-W/C}_{60}$ heterostructures. The antidamping is accompanied by a gigantic $\sim 115\%$ enhancement in the spin-pumping-induced output voltage owing to molecular hybridization. The noncollinear density-functional-theory calculations confirm the long-range enhancement of the SOC of $\beta\text{-W}$ upon the chemisorption of C_{60} molecules, which in turn can also enhance the SOC at the CFB/ $\beta\text{-W}$ interface in CFB/ $\beta\text{-W/C}_{60}$ heterostructures. The combined amplification of the bulk as well as the interfacial SOC upon molecular hybridization stabilizes the antidamping and enhanced spin-to-charge conversion, which can pave the way for the fabrication of power-efficient spintronic devices.

DOI: 10.1103/PhysRevApplied.21.054001

I. INTRODUCTION

Spintronic logic and memory devices have proven to be one of the most suitable research domains to meet the ultralow-power-consumption demand in the post-complementary metal oxide semiconductor (post-CMOS) technology era. Especially, with the advent of artificial intelligence and the Internet of Things, the further scaling down of CMOS technology can reach its physical limits in size, speed, and static energy consumption. The conceptualized spin-orbit torque magnetic random-access memory (SOT-MRAM) devices, which take advantage of the spin Hall effect (SHE), can bring down the energy consumption from the picojoule to the femtojoule scale [1,2]. The SHE-based magnetization switching mechanism in SOT-MRAMs also offers much improved endurance owing to the separation of the data writing and reading paths. Though these potentials of SOT-MRAMs have attracted

major attention, several challenges need to be addressed before the commercialization of SOT-MRAMs [1,2].

The increase of writing efficiency to reduce power consumption is one of those aspects which requires significant consideration. In this context, the spin Hall angle θ_{SH} (J_S/J_C) of the nonmagnetic layer present in the SOT-MRAMs, where J_C and J_S are the charge and spin current densities, respectively, plays a critical role in determining the writing efficiency [3]. Efficient charge-to-spin interconversion can lead to faster switching of the magnetization of the adjacent magnetic layer via SHE. Hence, various types of heavy metals (HMs), like Pt, Ta, W, Ir, etc., have been investigated in the past two decades to reduce the power consumption of future spintronic devices [4–6]. On a similar note, the Rashba-Edelstein effect (REE) occurring at the interfaces with spatial inversion symmetry breaking and high spin-orbit coupling (SOC) also has the potential for the manifestation of efficient charge-to-spin interconversion [7–9]. Hence, the combination of SHE and REE can be the most suitable alternative for the development of power-efficient spintronic applications.

*Corresponding author: ehesan.ali@inst.ac.in

†Corresponding author: sbedanta@niser.ac.in

Among all the heavy metals, highly resistive ($\rho_{\beta\text{-W}} \sim 100\text{--}300 \mu\Omega \text{ cm}$) metastable β -W possesses the largest $\theta_{\text{SH}} \sim -0.3$ to -0.4 [10–14], which makes it a strong candidate for SOT-MRAM devices. Usually, additional reactive gases, like O₂, N₂, and F, are employed to stabilize the A15 crystal structure of β -W [11] and, consequently, a larger θ_{SH} is realized. For example, Demasius *et al.* have been able to achieve $\theta_{\text{SH}} \sim -0.5$ by incorporating oxygen into tungsten thin films [12]. Interface engineering also acts as a powerful tool for enhancing the writing efficiency in β -W-based SOT-MRAM devices [15–17]. For instance, the presence of an interfacial atomically thin α -W layer in CoFeB/ α -W/ β -W trilayer suppresses the spin backflow current, resulting in a 45% increase in the spin mixing conductance [15]. Further, the REE evolved at the W/Pt interface owing to spin accumulation generates an additional spin-orbit field on the adjacent ferromagnetic NiFe (Permalloy, Py) layer [18]. The coexistence of SHE and REE has also been reported in CoFeB/ β -Ta and NiFe/Pt bilayers, where the interfacial SOC arising at the ferromagnet (FM)/HM interface plays a vital role in the spin-to-charge interconversion phenomenon [19,20].

More interestingly, a recent theoretical work has predicted that the interfacial SOC-mediated spin Hall angle of Pt can be 25 times larger than the bulk value in a NiFe/Pt heterostructure [21]. Interfacial SOC-mediated spin accumulation has also been reported to occur at the Rashba-like β -Ta/Py interface without dc current flow [22]. The spin pumping induced by the ferromagnetic resonance results in nonequilibrium spin accumulation at the interface, which consequently reduces the effective Gilbert damping of the β -Ta/Py bilayer. The reduction in effective damping, also termed antidamping, is similar to the interfacial Rashba-like SOT, observed in various HM/FM heterostructures [22]. The antidamping phenomenon without the requirement of dc current depends on several factors, like SOC of HM, strength of built-in electric field at the interface, interface quality, etc. Hence, the interface engineering via tuning the interfacial SOC in β -W-based HM/FM heterostructures can be the path forward for developing power-efficient SOT-MRAM devices.

To date, most interface engineering research has been focused on employing an additional metallic or oxide layer in the HM/FM system for the enhancement of spin-to-charge interconversion efficiency. However, organic semiconductors (OSCs) can also be incorporated in the HM/FM system to fabricate hybrid power-efficient spintronic devices owing to their strong interfacial hybridization and charge-transfer nature at the metal/OSC interface [23]. Recently, the SOC of Pt has been found to be enhanced due to the on-surface physical adsorption of C₆₀ (fullerene) molecules in yttrium iron garnet (YIG)/Pt/C₆₀ trilayers [24]. However, the θ_{SH} of Pt is usually found to be smaller compared to that of β -W and it is important to investigate the magnetization dynamics and

spin-to-charge conversion phenomena in FM/ β -W/C₆₀ heterostructures.

Hence, in this paper, we report the effect of molecular hybridization at the β -W/C₆₀ interface on magnetization dynamics and spin-to-charge conversion phenomena in Co₂₀Fe₆₀B₂₀ (CFB)/ β -W/C₆₀ heterostructures. Molecular hybridization reduces the effective Gilbert damping and also enhances the spin-to-charge conversion efficiency owing to the enhanced SOC of β -W and consequent strengthening of possible Rashba-like interaction at the CFB/ β -W interface. The strong chemisorption at the β -W/C₆₀ interface and the evolution of enhanced SOC of β -W upon molecular hybridization have also been confirmed by calculations based on first-principles density-functional theory (DFT).

II. EXPERIMENTAL AND COMPUTATIONAL METHODS

Four different types of heterostructures with CFB (7 nm)/ β -W (2.5, 5 nm) [Fig. 1(a)] and CFB (7 nm)/ β -W (2.5, 5 nm)/C₆₀ (13 nm) [Fig. 1(b)] stacks were fabricated on Si/SiO₂ (300 nm) substrates for the investigation of magnetization dynamics and spin-pumping phenomena. In addition, CFB (7 nm)/ β -W (10, 13 nm) heterostructures were also fabricated to reaffirm the stabilization of β -W. The heterostructure stacks and their nomenclature are listed in Table I.

The CFB and β -W layers were grown by dc magnetron sputtering, while an effusion cell equipped in a separate chamber (manufactured by EXCEL Instruments, India) was used for the growth of the C₆₀ overlayers in the CFWC

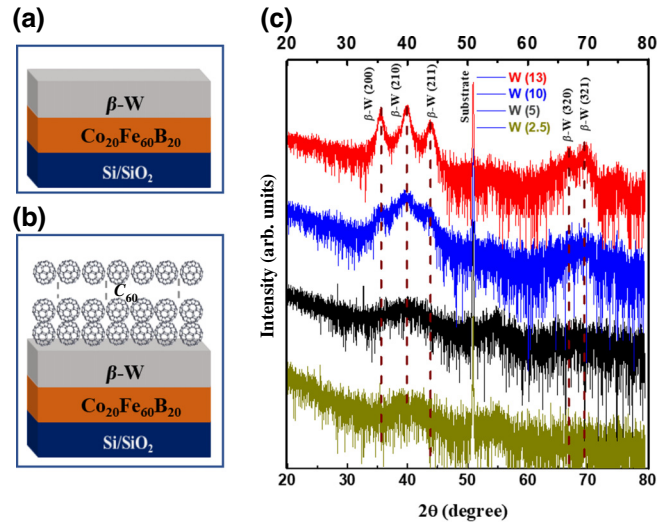


FIG. 1. Schematics of the (a) Si/SiO₂/CFB/ β -W and (b) Si/SiO₂/CFB/ β -W/C₆₀ heterostructures. (c) GIXRD patterns of the Si/SiO₂/CFB/ β -W heterostructures with various thicknesses of β -W.

TABLE I. Details of the heterostructures and their nomenclature.

No.	Stacking	Nomenclature
1	Si/SiO ₂ (300 nm)/CFB (7 nm)/ β -W (2.5 nm)	CFW1
2	Si/SiO ₂ (300 nm)/CFB (7 nm)/ β -W (5 nm)	CFW2
3	Si/SiO ₂ (300 nm)/CFB (7 nm)/ β -W (2.5 nm)/C ₆₀ (13 nm)	CFWC1
4	Si/SiO ₂ (300 nm)/CFB (7 nm)/ β -W (5 nm)/C ₆₀ (13 nm)	CFWC2

series. While preparing CFWC1 and CFWC2, the samples were transferred *in situ* into the chamber with effusion cells in a vacuum of $\sim 10^{-8}$ mbar for the deposition of C₆₀. Before the fabrication of heterostructures, thin films of CFB, β -W, and C₆₀ were prepared for thickness calibration and study of magnetic and electrical properties. The base pressures of the sputtering chamber and of the chamber with effusion cells were usually maintained at $\sim 4 \times 10^{-8}$ and $\sim 6 \times 10^{-9}$ mbar, respectively.

The structural characterizations of individual thin films and heterostructures were performed by x-ray diffraction (XRD), x-ray reflectivity (XRR), and Raman spectrometry. A magneto-optic Kerr effect-based microscope and superconducting quantum interference device-based vibrating sample magnetometer (SQUID-VSM) were employed for the static magnetization characterization and magnetic domain imaging. The magnetization dynamics was investigated by a lock-in based ferromagnetic resonance (FMR) spectrometer manufactured by NanOsc, Sweden. The heterostructures were kept in a flip-chip manner on a coplanar waveguide (CPW). The FMR spectra were recorded in the 4–17 GHz range for all the samples. The FMR spectrometer setup is also equipped with an additional nanovoltmeter using which spin-to-charge conversion phenomena of all the devices were measured via inverse spin Hall effect (ISHE) with 5–22 dBm rf power. The contacts were made at the two opposite ends of $3 \times 2 \text{ mm}^2$ devices using silver paste to measure the ISHE-induced voltage drop across the samples. The details of the ISHE measurement setup are mentioned elsewhere [25,26].

DFT-based electronic-structure calculations were performed in the Vienna *Ab initio* Simulation Package (VASP) [27,28] to understand the interface's chemical bonding and surface reconstructions. The plane-wave basis sets expand the valence electronic states, and the core electrons are treated with pseudopotentials. The core-valence interactions are considered with the projected augmented-wave method. The exchange-correlation potentials are treated with a Perdew-Burke-Ernzerhof [29] functional which inherits the generalized gradient approximation. This functional produces a reliable understanding of similar kinds of interfaces. The convergence of the self-consistent field iterations was ensured with a plane-wave cutoff energy of 500 eV and a tolerance of 10^{-6} eV/cycle. A D3 dispersion correction term, devised by Grimme, that accounts

for the long-range interaction terms was employed in the calculations.

The optimized unit-cell parameter obtained from the aforementioned methods for the cubic A15 crystal of β -W is 5.014 Å, which resembles the experimental parameter of 5.036 Å. The (210) surface unit cell of β -W is used to construct the model substrate. We have only considered the β -W/C₆₀ stacking in our calculations. As the CFB layer is amorphous in nature, it is difficult to construct a simulation supercell with CFB. Hence, it is not included in the DFT calculations. Further, the thickness of the W film for DFT calculation has been chosen to be thinner than in the experiment due to computational constraints. The (210) surface is repeated twice along the crystallographic *b* axis of the surface unit cell. This extended surface supercell is repeated five (10) times along the (210) surface normal to model the substrate supercell of thickness 1.065 nm (2.10 nm). A vacuum of 30 Å is added along the crystallographic *c* axis to ensure no interaction between the supercells along the surface direction. The lower two atomic layers were fixed at the bulk, and the remaining layers were allowed to relax during the geometry optimization. One unit of the C₆₀ molecule is adsorbed per supercell of the β -W substrate. To understand the effect of the spin-orbit coupling interactions, we have performed noncollinear DFT calculations as implemented in VASP. The calculated E_{SOC} value quantifies the strength of the SOC term in the Hamiltonian.

III. RESULTS AND DISCUSSION

Grazing-incidence x-ray diffraction (GIXRD) was performed for all the heterostructures. The XRD patterns of the CFB/ β -W heterostructures with different thicknesses of β -W are shown in Fig. 1(c). The presence of (200), (210), and (211) Bragg peaks of W at 35.5°, 39.8°, and 43.5° indicates the stabilization of the β phase of W (A15 crystal structure) [5,30]. In addition, we have also observed the (320) and (321) Bragg peaks of W, which further suggests the growth of polycrystalline β -W. The relative intensities of the (320) and (321) Bragg peaks of W are lower compared to those of the (200), (210), and (211) Bragg peaks, consistent with previous reports [30]. The Bragg peaks are more prominent for heterostructures with thicker W layers, as diffraction intensity increases with increase in W thickness. The XRD patterns for CFWC1 and CFWC2 are similar to those for CFW1 and CFW2,

respectively, as the thicknesses of β -W are the same. Here, we have not used reactive gases like O₂ and N₂ for the growth of β -W, unlike previous reports [11,12].

The resistivity of W films with thicknesses of 2.5, 5, and 10 nm were measured by standard four-probe methods. The resistivity decreases with increase in thickness of W and were found to be \sim 300–100 $\mu\Omega$ cm, further confirming the growth of the β phase of W [5,30]. We also do not observe the (110), (200), and (211) Bragg peaks for bcc α -W in the XRD patterns and α -W would also have exhibited one order less resistivity compared to what we have observed [30]. The stabilization of the pure β phase of W is quite important for future SOT device fabrication and hence we can expect a high spin-to-charge conversion efficiency in our CFB/ β -W heterostructures owing to the high SOC of β -W [10,30].

The XRR measurements were performed for all the samples in both the CFW and CFWC series to confirm the desired thickness of individual layers and to investigate the interface quality. Figure S1 in the Supplemental Material shows the XRR patterns of all the heterostructures considered for the present study [31]. The experimental data were fitted using GenX software and the simulated patterns are also shown in Fig. S1 (red curves). The presence of Kiessig oscillations for all the films implies the absence of a high degree of interfacial disorder and dislocations. The relative peak positions and intensities of the simulated patterns agree quite well with the experimentally observed low-angle XRR data. The fit provides the anticipated thickness of individual layers in each sample as mentioned in Table I. The interface roughness for all the heterostructures was found to be in the range of 0.2–0.5 nm, further indicating the high-quality growth of both series of samples.

Figure S2 in the Supplemental Material displays the Raman spectrum of 13-nm C₆₀ film grown on the Si/SiO₂ (300 nm) substrate under the same growth conditions as in the heterostructures [31]. The presence of the A_g (2) and H_g (8) Raman modes of C₆₀ around \sim 1460 and 1566 cm⁻¹, respectively, confirms the growth of the C₆₀ film [32,33]. In addition, the Raman mode around \sim 495 cm⁻¹ corresponding to the A_g (1) mode of C₆₀ is also observed in the Raman spectrum. The anticipated thickness of C₆₀ in the C₆₀ thin film, CFWC1, and CFWC2 has also been confirmed from the XRR measurements. The Raman spectrum of our C₆₀ film grown by effusion cells is quite similar to those prepared by different solution methods in HCl or N₂ atmosphere [32,33].

The saturation magnetization and the magnetic domain images of all the heterostructures are found to be similar (see Supplemental Material), as the bottom CFB layer is the same for all the heterostructures [31,34,35]. The magnetization relaxation and propagation of spin angular momentum in the CFB thin film and the heterostructures in both the CFW and CFWC series were studied to explore the effect of the highly resistive β -W and β -W/C₆₀ bilayer

by the in-plane FMR technique. The heterostructures are placed in a flip-chip manner on CPW, as shown in the schematic in Fig. S4(a) in the Supplemental Material [31]. Figure S4(c) shows the typical FMR spectra of CFW1 and CFWC1 heterostructures measured in the 4–17 GHz range [31].

All the FMR spectra were fitted to the derivative of symmetric and antisymmetric Lorentzian functions to evaluate the resonance field (H_{res}) and linewidth (ΔH) [36]:

$$\begin{aligned} \text{FMR signal} = & K_1 \frac{4\Delta H(H - H_{\text{res}})}{[(\Delta H)^2 + 4(H - H_{\text{res}})^2]^2} \\ & - K_2 \frac{(\Delta H)^2 - 4(H - H_{\text{res}})^2}{[(\Delta H)^2 + 4(H - H_{\text{res}})^2]^2} + \text{offset}, \end{aligned} \quad (1)$$

where K_1 and K_2 are the antisymmetric and symmetric absorption coefficients, respectively.

The extracted H_{res} and ΔH values at different resonance frequencies (f) of all the heterostructures are shown in Figs. 2(a) and 2(b). The f versus H_{res} of different samples in the CFW and CFWC series are plotted in Fig. 2(a). The f versus H_{res} plots are fitted by using Eq. (2) [36]:

$$f = \frac{\gamma}{2\pi} \sqrt{(H_K + H_{\text{res}})(H_K + H_{\text{res}} + 4\pi M_{\text{eff}})}, \quad (2)$$

where

$$4\pi M_{\text{eff}} = 4\pi M_S + \frac{2K_S}{M_S t_{\text{FM}}}$$

and H_K , K_S , and t_{FM} are the anisotropy field, perpendicular surface anisotropy constant, and the thickness of FM, respectively. Here, γ is the gyromagnetic ratio, and $4\pi M_{\text{eff}}$ represents the effective magnetization. The $4\pi M_{\text{eff}}$ value extracted from the fitting gives similar values as compared with the saturation magnetization value ($4\pi M_S$) calculated from the SQUID-VSM.

Further, the effective Gilbert damping constant (α_{eff}) and hence the magnetization relaxation mechanism are studied from the resonance-frequency-dependent FMR linewidth behavior. The ΔH versus f plots are shown in Fig. 2(b). The linear dependence of ΔH on f indicates that the magnetic damping is mainly governed by the intrinsic mechanism via electron-magnon scattering rather than the extrinsic two-magnon scattering. The ΔH versus f plots are fitted by the following linear equation [36] to evaluate α_{eff} :

$$\Delta H = \Delta H_0 + \frac{4\pi\alpha_{\text{eff}}}{\gamma} f, \quad (3)$$

where ΔH_0 is the inhomogeneous linewidth broadening. The α_{eff} values for all the heterostructures and CFB thin film obtained from the fitting are shown in Table II.

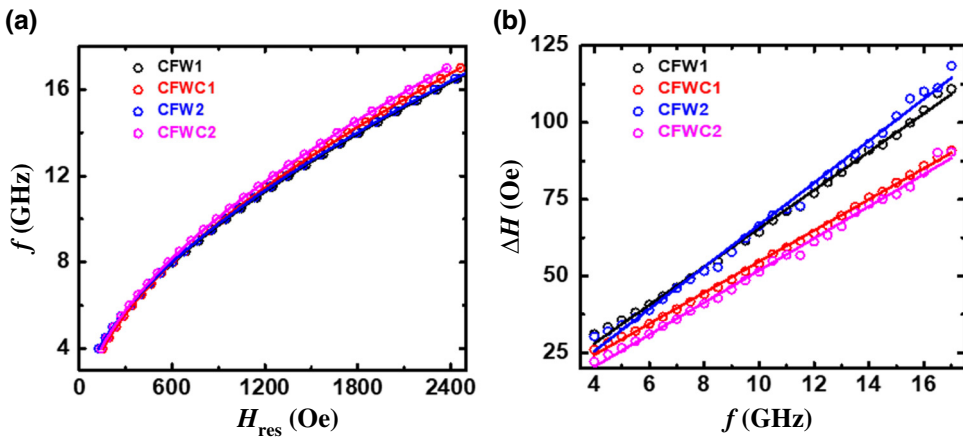


FIG. 2. (a) Frequency (f) versus resonance field (H_{res}) and (b) linewidth (ΔH) versus frequency (f) behavior for various heterostructures. The solid lines are the best fits to Eqs. (2) and (3).

The α_{eff} value for the CFW series ($\sim 0.0075 \pm 0.0001$ for CFW1 and $\sim 0.0080 \pm 0.0001$ for CFW2) are found to be larger compared to that of the CFB thin film ($\sim 0.0059 \pm 0.0001$). The enhancement of α_{eff} indicates the possible evolution of the spin-pumping mechanism in the CFB/ β -W bilayers. Interestingly, α_{eff} decreases to $\sim 0.0065 \pm 0.0001$ upon the deposition of C_60 molecules on CFB/ β -W bilayers in the CFWC series. The significant change in α_{eff} for the CFB/ β -W/ C_60 heterostructures compared to CFB/ β -W bilayers indicates the modification of the physical properties of β -W layer in CFB/ β -W/ C_60 .

The crossover observed for the CFW1 and CFW2 heterostructures can be mainly ascribed to the different α_{eff} values and consequently different slopes of the linear fit for both heterostructures in Fig. 2(b). The α_{eff} values for CFWC1 and CFWC2 are quite similar (Table II) and hence the slope of the ΔH versus f plots does not change much. This leads to the absence of crossover for CFWC1 and CFWC2 heterostructures in Fig. 2(b). The deposition of C_60 molecules can lead to metal/molecule hybridization at the β -W/ C_60 interface, which in turn can alter the properties of β -W.

First-principles DFT-based calculations were performed to elucidate further the molecular hybridization at the

β -W/ C_60 interface and its consequences on the magnetization dynamics of CFB/ β -W/ C_60 heterostructures. The extended simulation supercell for C_60 on β -W(210) is shown in Fig. 3(a). The C_60 molecule is observed as strongly chemisorbed onto the β -W(210) surface with an adsorption energy of -253.5 kcal/mol. The adsorption energy is quite high compared to those of the other substrates. For example, the adsorption energy for Co/ C_60 was found to be -90 kcal/mol [37] while for the Pt/ C_60 interface it is reported to be -115 kcal/mol [38].

The chemisorption in the case of β -W/ C_60 is quite strong and induces distortion to the spherical shape of the adsorbed C_60 . The distance between the two carbon atoms from two opposite hexagons of adsorbed C_60 is shorter along one direction compared to the other measured in the plane [left panel of Fig. 3(a)]. The diameter of C_60 molecules decreases by 0.3 Å when it is measured perpendicular to the β -W(210) surface [right panel of Fig. 3(a)]. This distortion can be attributed to W—C bond formation due to the strong chemisorption at the β -W/ C_60 interface. This chemisorption strongly alters the electronic structure of the β -W and C_60 molecule [Fig. 3(b)]. The p_z orbital, which accommodates the π electrons of the C_60 , hybridizes with the d orbitals of the β -W atom and forms hybridized interfacial states. The out-of-plane d orbitals (d_{xz} , d_{yz} , and d_{z^2} orbitals) are strongly hybridized with the p_z orbital of the carbon atom over a large energy window near the Fermi energy level (see Fig. 3 and Fig. S5 in the Supplemental Material) [31].

The sharp peaks observed in the density of states of the free C_60 layer get significantly broadened, flattened, and shifted for β -W/ C_60 stacking. The strong metallo-organic hybridization also modifies the partial density of states of the various d orbitals of β -W. The d orbitals become flattened and spread over a larger energy spectrum around the Fermi level upon molecular hybridization. The formation of the W—C bond also costs a transfer of

TABLE II. Effective Gilbert damping, spin mixing conductance, and symmetric component of measured dc voltage for different heterostructures.

Hetero-structure	α_{eff} (± 0.0001)	$g_{\text{eff}}^{(\uparrow\downarrow)}$ (10^{19} m^{-2})	V_{SYM} (μV)
CFB	0.0059
CFW1	0.0075	0.87	1.08
CFW2	0.0080	1.13	1.25
CFWC1	0.0064	0.27	2.32
CFWC2	0.0065	0.32	1.78

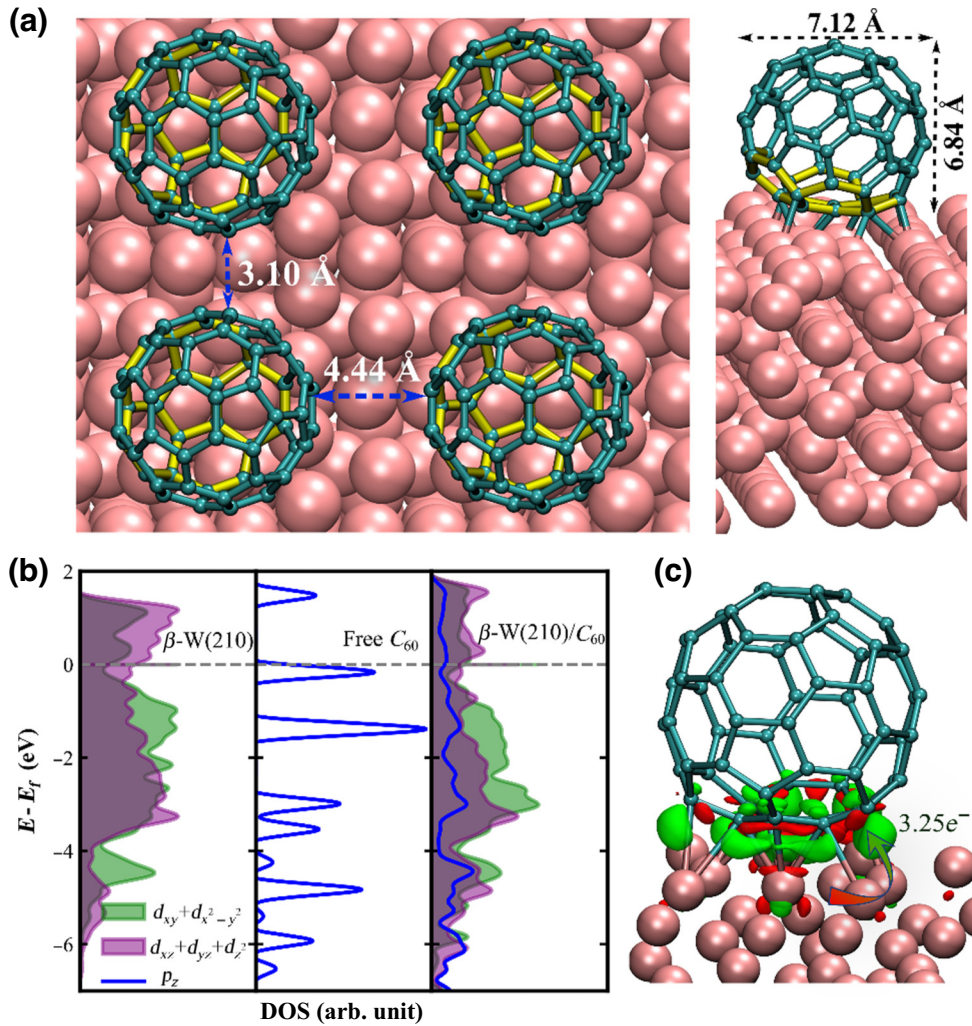


FIG. 3. (a) The extended simulation supercell for the C₆₀ on β-W(210) substrate. The left panel shows the top view of the surface supercell (along the z axis), and the right panel shows the side view of the same. The larger pink balls and the smaller cyan balls represent the tungsten and carbon atoms, respectively. The yellow bonds highlight the section of the C₆₀ that takes part in interface formation. The double-headed dashed black arrows quantify the diameter of the C₆₀ spheres in two directions. (b),(c) The modification in the electronic structure due to chemisorption of the C₆₀ molecule on the β-W. (b) The atom projected orbital resolved partial density of states of β-W(210), C₆₀, and β-W(210)/C₆₀. (c) The electron density redistribution due to chemisorption. The red and green isosurfaces depict electron density depletion and accumulation of the electron density at the interface, respectively. The curved bi-colored arrow depicts the direction of the electron transfer process.

3.25e⁻ from the interfacial layer of the β-W to the C₆₀ molecule [Fig. 3(c)]. This is relatively higher compared to the previously reported 0.25e⁻ transfer from Pt(111) and 3e⁻ transfer from Cu(111) to the adjacent C₆₀ molecule, meaning that the metallo-organic hybridization is rather stronger in the case of the β-W/C₆₀ interface [38]. Hence, the molecular hybridization of β-W is expected to alter its physical properties with greater effect and can be considered as an important tool to optimize spintronic device performance.

The modified electronic structure was found to exert a long-range effect on the strength of the spin-orbit coupling. The E_{SOC} values of bare β-W and β-W covered with C₆₀ molecules and the variation of E_{SOC} (i.e., ΔE_{SOC}) due to

β-W/C₆₀ hybridization are shown in Fig. 4. The interfacial W atoms involved in the hybridization with C₆₀ show a decrease in E_{SOC} . The rest of the W atoms from the surface layer exhibit an increase in E_{SOC} . The lower atomic layers of W also show an increment in E_{SOC} . The W layer farthest from the β-W/C₆₀ interface exhibits the most increased E_{SOC} , indicating that the enhancement of SOC can be a long-range effect in nature.

To further confirm the long-range effect of molecular hybridization, we have also performed DFT calculations for a β-W (2.1 nm)/C₆₀ bilayer. The enhancement in the SOC of β-W is still evident down to the tenth layer (last layer) away from the β-W/C₆₀ interface (see Figs. S6 and S7 in the Supplemental Material) [31]. The

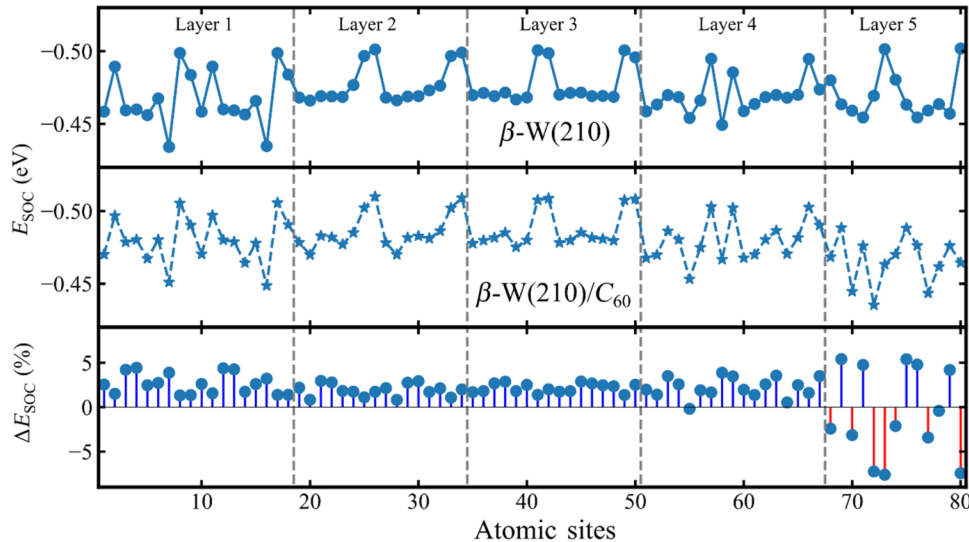


FIG. 4. The effect of chemisorption of the C_{60} molecule at the β -W(210) surface on E_{SOC} of various atomic sites. The percentage change in E_{SOC} (i.e., ΔE_{SOC}) is calculated in terms of the change in E_{SOC} of the bare β -W(210) substrate. Layer 5 is the interfacial layer that interacts with the C_{60} , and layer 1 is opposite to the β -W/ C_{60} interface layer.

hybridization at the β -W/ C_{60} interface increases the overall spin-orbit coupling strength of the β -W layer. Further, molecular hybridization has a long-range effect on the SOC of β -W. Hence, the enhancement of SOC due to the β -W/ C_{60} interface can interfere with the CFB/ β -W interface and modulate the interfacial SOC at the CFB/ β -W interface. The enhanced bulk SOC of β -W and the modulation of interfacial SOC at the CFB/ β -W interface can facilitate an efficient spin-to-charge conversion in CFB/ β -W/ C_{60} heterostructures.

The decrease in damping, usually known as antidamping, has been observed previously in FM/HM bilayers [22,26,30]. In those systems, the effective damping values become lower than the α_{eff} of the FM layer and this phenomenon has been attributed to the formation of Rashba-like interfacial states [22,30]. A similar type of evolution of Rashba-like states at the CFB/ β -W interface can be expected due to structural inversion asymmetry and the large SOC of β -W. Spin accumulation at the CFB/ β -W interface can lead to evolution of nonequilibrium spin states. The nonequilibrium spin states along with the enhanced SOC at the CFB/ β -W interface due to molecular hybridization as confirmed from the DFT calculations can generate an additional charge current due to the inverse Rashba-Edelstein effect (IREE) and can also induce the antidamping torque on the magnetization of the FM layer. The antidamping torque can make the magnetization precession relatively slower and thus, can decrease the α_{eff} of the CFB/ β -W/ C_{60} heterostructures compared to the CFB/ β -W bilayer.

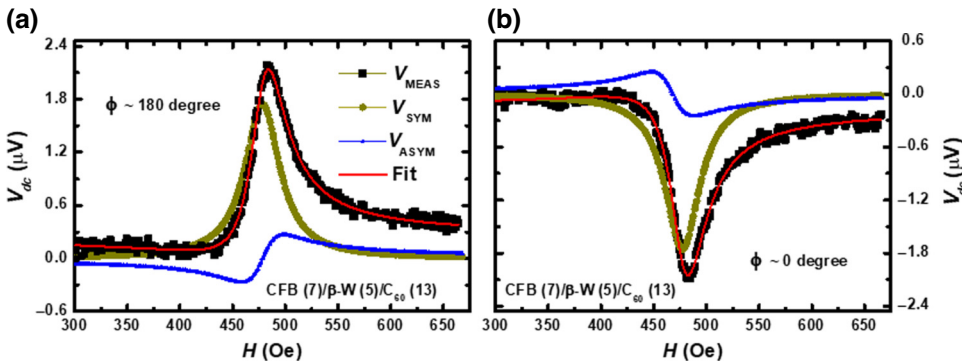
The control of Gilbert damping of FMs by interfacing with adjacent nonmagnetic metal/organic bilayers can also provide an alternative to the search for low-damping

magnetic materials. Especially, the low cost and abundant availability of carbon-based organic molecules can be commercially beneficial in optimizing the magnetic damping for spintronic applications. Further, Gilbert damping modulation can also control the effective spin mixing conductance ($g_{eff}^{(\uparrow\downarrow)}$) of the heterostructures which also plays a vital role for efficient spin current transport across the interface. Hence, the $g_{eff}^{(\uparrow\downarrow)}$ values of all the heterostructures were calculated from the damping constant measurement by Eq. (4) [36]:

$$g_{eff}^{(\uparrow\downarrow)} = \frac{4\pi M_S t_{CFB}}{g \mu_B} (\alpha_{CFB/NM} - \alpha_{CFB}). \quad (4)$$

Here g , μ_B , and t_{CFB} are the Landé g factor (2.1), Bohr magneton, and thickness of the CFB layer, respectively; $\alpha_{CFB/NM}$ is the damping constant of bilayers or trilayers; and α_{CFB} is the damping constant of the reference CFB thin film. The $g_{eff}^{(\uparrow\downarrow)}$ values for CFW1 and CFW2 (Table II) are relatively higher compared to previous reports on FM/ β -W bilayers. In particular, the $g_{eff}^{(\uparrow\downarrow)}$ of CFW2 is one order of magnitude higher than that reported for Py/ β -W bilayer ($1.63 \times 10^{18} \text{ m}^{-2}$) [30], and two orders higher compared to that of YIG/ β -W ($5.98 \times 10^{17} \text{ m}^{-2}$) [14]. This indicates the absence of any significant amount of spin backflow from the β -W layer and high SOC strength of the parent β -W layer in our system. However, the $g_{eff}^{(\uparrow\downarrow)}$ values decrease for the CFWC1 and CFWC2 trilayers owing to the antidamping phenomenon.

The ISHE measurements were performed for all the heterostructures in the CFW and CFWC series to gain more insights about the effect of molecular hybridization in CFB/ β -W/ C_{60} on the magnetization dynamics and



spin-to-charge conversion efficiency. Figure 5 shows the typical field-dependent dc voltage (V_{dc}) measured across the CFB (7 nm)/ β -W (5 nm)/C₆₀ (13 nm) heterostructure under FMR conditions. In order to separate the symmetric (V_{SYM}) and asymmetric (V_{ASYM}) components, the V_{dc} versus H plots were fitted with the following Lorentzian function:

$$V_{dc} = V_{SYM} \frac{(\Delta H)^2}{(\Delta H)^2 + (H - H_{res})^2} + V_{ASYM} \frac{\Delta H(H - H_{res})}{(\Delta H)^2 + (H - H_{res})^2}. \quad (5)$$

The extracted field-dependent V_{SYM} and V_{ASYM} are also plotted in Fig. 5. Similar types of field-dependent V_{MEAS} , V_{SYM} , and V_{ASYM} are also observed for other samples in both the CFW and CFWC series. The main contributions to V_{SYM} are from the spin-pumping voltage (V_{ISHE}) and the spin rectification effects arising from the anisotropic magnetoresistance (AMR; V_{AMR}) [36]. In contrast, the asymmetric component of the measured voltage arises solely due to the anomalous Hall effect and AMR [36]. The sign of V_{SYM} is reversed when ϕ [the angle between the perpendicular direction to the applied magnetic field (H) and the direction of voltage measurement] is changed from 0° to 180° (Fig. 5), confirming the presence of ISHE in our heterostructures.

The field-dependent V_{SYM} values for all four heterostructures are plotted in Figs. 6(a) and 6(b). Interestingly, the V_{SYM} value at the resonance field for CFB/ β -W/C₆₀ trilayers is found to be increased compared to that for CFB/ β -W bilayers. The increment is $\sim 115\%$ for β -W thickness 2.5 nm, while it becomes $\sim 20\%$ for β -W thickness 5 nm. The gigantic enhancement of V_{SYM} for CFB (7 nm)/ β -W (2.5 nm)/C₆₀ (13 nm) implies the modification of SOC of β -W when capped with organic C₆₀ molecules and the presence of an additional spin-to-charge conversion effect in the heterostructures.

Power-dependent spin-to-charge conversion measurements were also performed to further confirm the enhancement of V_{SYM} . The spin-pumping-induced voltage increases linearly with the rf power as shown in

FIG. 5. Plots of V_{MEAS} , V_{SYM} , and V_{ASYM} versus H for CFB (7 nm)/ β -W (5 nm)/C₆₀ (13 nm) (CFWC2) heterostructure with (a) $\phi \sim 180^\circ$ and (b) $\phi \sim 0^\circ$ measured at 15 dBm rf power. The red curve is a Lorentzian fit with Eq. (5) to V_{dc} versus H .

Fig. 6(c) for both CFW1 and CFWC1. The V_{SYM} value at different rf power is found to be increased for CFWC1 compared to CFW1, which further confirms the molecular-hybridization-induced enhanced spin-to-charge conversion. As the thickness and the magnetic properties of the bottom CFB layer are the same for all the heterostructures, the contribution of V_{AMR} is expected to be the same for CFB (7 nm)/ β -W (2.5 nm)/C₆₀ (13 nm) and CFB (7 nm)/ β -W (2.5 nm). Hence, the sizeable increase in the measured voltage can be attributed to the enhanced SOC of β -W due to molecular hybridization and additional charge current flowing at the CFB/ β -W interface due to IREE, as shown in Fig. 6(d).

In order to understand the enhanced spin-to-charge conversion phenomenon further, we also calculated θ_{SH} of the heterostructures by using Eqs. (6) and (7) [14,36]:

$$J_S = \frac{g_{eff}^{(\uparrow\downarrow)} \gamma^2 h_{rf}^2 \hbar [\gamma 4\pi M_S + \sqrt{(\gamma 4\pi M_S)^2 + 4\omega^2}]}{8\pi\alpha_{eff}^2 [(\gamma 4\pi M_S)^2 + 4\omega^2]} \times \left(\frac{2e}{\hbar} \right), \quad (6)$$

$$V_{ISHE} = \frac{w_y L \rho_{NM}}{t_{NM}} \theta_{SH} \lambda_{NM} \tanh \left(\frac{t_{NM}}{2\lambda_{NM}} \right) J_S, \quad (7)$$

where ρ_{NM} is the resistivity of the β -W measured by four-probe technique and L is the length of the sample. The rf field (h_{rf}) and the width of the CPW transmission line (w_y) in our measurements are 0.5 Oe (at 15 dBm rf power) and 200 μ m, respectively. The value of spin diffusion length (λ_{NM}) for β -W has been taken as ~ 3 nm from the literature [39].

Angle-dependent ISHE measurements were performed to separate the AMR contribution from V_{SYM} [40]. The contribution of V_{AMR} was found to be one order smaller compared to V_{ISHE} . For example, V_{AMR} and V_{ISHE} for the CFW2 heterostructure are found to be ~ 0.15 and ~ 1.25 μ V, respectively (see the Supplemental Material) [31]. The ρ_{NM} value for 5 nm β -W is found to be 250 $\mu\Omega$ cm. Hence, θ_{SH} for the CFB (7 nm)/ β -W (5 nm) bilayer estimated using Eqs. (6) and (7) is found to be $\sim -0.6 \pm 0.01$. A similar calculation for the

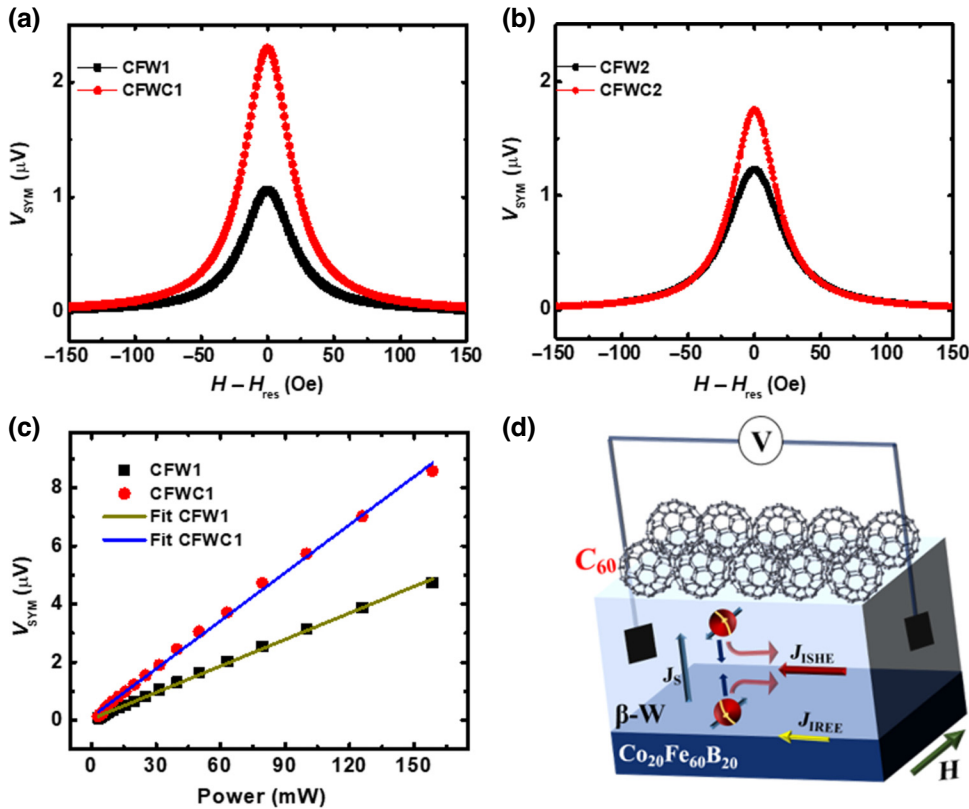


FIG. 6. Plots of V_{SYM} versus applied magnetic field with $\phi \sim 180^\circ$ for (a) CFB (7 nm)/ β -W (2.5 nm) (CFW1) and CFB (7 nm)/ β -W (2.5 nm)/ C_60 (13 nm) (CFWC1) and (b) CFB (7 nm)/ β -W (5 nm) (CFW2) and CFB (7 nm)/ β -W (5 nm)/ C_60 (13 nm) (CFWC2) heterostructures measured at 15 dBm rf power. (c) Power-dependent V_{SYM} for CFW1 and CFWC1 (the solid line is the linear fit). (d) Schematic showing the spin-to-charge conversion phenomenon in CFB/ β -W/ C_60 heterostructures.

CFB (7 nm)/ β -W (2.5 nm) bilayer estimates θ_{SH} to be $\sim -0.67 \pm 0.01$. The observed θ_{SH} value is larger compared to that reported in the literature [10–12]. The high SOC of our β -W and higher spin-mixing conductance could be responsible for this enhanced θ_{SH} .

Further, the interfacial SOC at the CFB/ β -W interface can also induce an additive spin-to-charge conversion effect, contributing to the enhancement of θ_{SH} . Such type of interfacial SOC-mediated enhanced spin-to-charge conversion has been reported previously for NiFe/Pt and CFB/ β -Ta [19,20]. Here, it is important to note that it is difficult to disentangle the IREE and ISHE effects in these types of FM/HM systems. On the other hand, $g_{\text{eff}}^{(\uparrow\downarrow)}$ for CFWC1 and CFWC2 decreases by 70% due to the antidamping phenomenon, and hence the reduction in J_S according to Eq. (6). However, V_{ISHE} for CFWC1 and CFWC2 are found to be larger than for CFW1 and CFW2, respectively (Fig. 6). This leads to the value of $\theta_{\text{SH}} > 1$, calculated using Eqs. (6) and (7) for CFB/ β -W/ C_60 heterostructures. This type of gigantic enhancement of θ_{SH} cannot be explained by mere bulk ISHE in β -W.

The enhanced θ_{SH} can be partly attributed to the enhanced bulk SOC of β -W upon molecular hybridization, as predicted by the DFT calculations. Further, our DFT

calculations also predict the enhancement of SOC of β -W down to the last layer away from the β -W/ C_60 interface. Hence, molecular hybridization has a long-range effect on the SOC of β -W. This can interfere with the CFB/ β -W interface and modulate the interfacial SOC at the CFB/ β -W interface. The long-range molecular hybridization effect can also tune the interfacial SOC at the CFB/ β -W interface due to its dependence on the orbital characters of the bands involved [41,42].

The larger interfacial SOC and inversion symmetry breaking at the CFB/ β -W interface make the scenario favorable for realizing an enhanced interfacial charge current due to the IREE, as depicted in Fig. 6(d). Hence, the combination of bulk SOC enhancement and IREE-induced spin-to-charge conversion due to the strong chemisorption of C_60 on β -W can contribute to the sizeable increase in θ_{SH} in CFB/ β -W/ C_60 heterostructures. There is also a possibility that the interaction at the β -W/ C_60 interface may decay as we move toward the FM/HM interface. However, a collective effect that spans over the β -W thickness region seems to be more arguable considering the significant enhancement of spin-pumping-induced output voltage in CFB/ β -W/ C_60 heterostructures.

The enhanced output dc voltage due to spin pumping upon C_{60} deposition on β -W is also consistent with the reduced effective damping value as discussed earlier. The enhanced SOC of β -W and the structural inversion asymmetry at the CFB/ β -W interface can stabilize the Rashba-like states at the FM/HM interface [19,20].

IREE-mediated spin-to-charge conversion has received considerable interest since its discovery at the Ag/Bi interface [7]. To date, most of the IREE effects have been experimentally realized at all-inorganic metal/metal, metal/oxide, or oxide/oxide interfaces [9]. Our experiments and theoretical calculations show that molecular hybridization at the HM/OSC interface can also help in strengthening the Rashba spin-orbit coupling at the FM/HM interface. The Rashba interaction leads to the spin splitting of bands, whose magnitude is dependent on the SOC strength at the interface. Upon molecular hybridization, the SOC strength of β -W is further enhanced. This could lead to a larger Rashba coefficient α_R and hence a relatively larger IREE at the FM/HM interface. The simultaneous observation of ISHE and IREE by engineering the HM interface with OSC can help in reducing the power consumption of future SOT-MRAM devices. As CFB/ β -W stacking is employed for fabrication of spin Hall nano-oscillators [43], incorporating organic molecules can also significantly enhance their efficiency. Hence, the HM/ C_{60} interface can reduce the power consumption for data storage as well as facilitate in performing efficient spin logic operations.

IV. CONCLUSION

In conclusion, a strong interfacial SOC can lead to larger spin Hall angle in CFB/ β -W bilayer. Thermally evaporated organic C_{60} molecules on a CFB/ β -W bilayer lead to strong chemisorption at the β -W/ C_{60} interface. The experimental and theoretical calculations confirm that molecular hybridization enhances the bulk as well as the interfacial SOC in CFB/ β -W/ C_{60} heterostructures. The strengthening of technologically important SOC manifests an antidamping phenomenon and gigantic ($\sim 115\%$) increase in spin-pumping-induced output voltage for CFB/ β -W/ C_{60} stacking. The control of magnetization dynamics and output efficiency in spintronic devices by molecular hybridization can be a viable alternative to other interface engineering and surface alloying techniques. The stabilization of antidamping and enhanced spin-to-charge conversion by tuning the bulk as well as interfacial SOC via employing cost-effective, abundant organic molecules can pave the way to the fabrication of next-generation power-efficient spintronic devices.

ACKNOWLEDGMENTS

S.B., A.S., and S.P.M. acknowledge the Department of Atomic Energy (DAE), the Department of Science and

Technology (DST) of the Government of India, and SERB project CRG/2021/001245. E.A. and A.M. acknowledge the SERB project CRG/2019/003237. A.S. acknowledges the DST-National Postdoctoral Fellowship in Nano Science and Technology. We are also grateful to the Center for Interdisciplinary Sciences, NISER, for providing the Raman spectroscopy measurement facility.

- [1] Z. Guo, J. Yin, Y. Bai, D. Zhu, K. Shi, G. Wang, K. Cao, and W. Zhao, Spintronics for energy-efficient computing: An overview and outlook, *Proc. IEEE* **109**, 1398 (2021).
- [2] R. Ramaswamy, J. M. Lee, K. Cai, and H. Yang, Recent advances in spin-orbit torques: Moving towards device applications, *Appl. Phys. Rev.* **5**, 031107 (2018).
- [3] Y. Wang, P. Deorani, X. Qiu, J. H. Kwon, and H. Yang, Determination of intrinsic spin Hall angle in Pt, *Appl. Phys. Lett.* **105**, 152412 (2014).
- [4] T. Fache, J. Rojas-Sánchez, L. Badie, S. Mangin, and S. Petit-Watelot, Determination of spin Hall angle, spin mixing conductance, and spin diffusion length in CoFeB/Ir for spin-orbitronic devices, *Phys. Rev. B* **102**, 064425 (2020).
- [5] S. Hait, S. Husain, H. Bangar, L. Pandey, V. Barwal, N. Kumar, N. K. Gupta, V. Mishra, N. Sharma, and P. Gupta, *et al.*, Spin pumping through different spin-orbit coupling interfaces in β -W/interlayer/Co₂FeAl heterostructures, *ACS Appl. Mater. Interfaces* **14**, 37182 (2022).
- [6] S.-I. Kim, D.-J. Kim, M.-S. Seo, B.-G. Park, and S.-Y. Park, Dependence of inverse-spin Hall effect and spin-rectified voltage on tantalum thickness in Ta/CoFeB bilayer structure, *Appl. Phys. Lett.* **106**, 032409 (2015).
- [7] J. R. Sánchez, L. Vila, G. Desfonds, S. Gambarelli, J. Attané, J. De Teresa, C. Magén, and A. Fert, Spin-to-charge conversion using Rashba coupling at the interface between non-magnetic materials, *Nat. Commun.* **4**, 2944 (2013).
- [8] H. Bangar, A. Kumar, N. Chowdhury, R. Mudgal, P. Gupta, R. S. Yadav, S. Das, and P. K. Muduli, Large spin-to-charge conversion at the two-dimensional interface of transition-metal dichalcogenides and permalloy, *ACS Appl. Mater. Interfaces* **14**, 41598 (2022).
- [9] H. C. Koo, S. B. Kim, H. Kim, T.-E. Park, J. W. Choi, K.-W. Kim, G. Go, J. H. Oh, D.-K. Lee, and E.-S. Park, *et al.*, Rashba effect in functional spintronic devices, *Adv. Mater.* **32**, 2002117 (2020).
- [10] X. Sui, C. Wang, J. Kim, J. Wang, S. Rhim, W. Duan, and N. Kioussis, Giant enhancement of the intrinsic spin Hall conductivity in β -tungsten via substitutional doping, *Phys. Rev. B* **96**, 241105 (2017).
- [11] O. L. McHugh, W. F. Goh, M. Gradhand, and D. A. Stewart, Impact of impurities on the spin Hall conductivity in β -W, *Phys. Rev. Mater.* **4**, 094404 (2020).
- [12] K.-U. Demasius, T. Phung, W. Zhang, B. P. Hughes, S.-H. Yang, A. Kellock, W. Han, A. Pushp, and S. S. Parkin, Enhanced spin-orbit torques by oxygen incorporation in tungsten films, *Nat. Commun.* **7**, 10644 (2016).
- [13] Y. Saito, N. Tezuka, S. Ikeda, H. Sato, and T. Endoh, Increase in spin-Hall effect and influence of anomalous Nernst effect on spin-Hall magnetoresistance

- in β -phase and α -phase $W_{100-x}Ta_x/CoFeB$ systems, *Appl. Phys. Express* **12**, 053008 (2019).
- [14] H. Bai, L. Jin, G. Li, J. Su, Z. Zhu, Y. Zhang, T. Zhu, H. Zhang, and J. Cai, Simultaneously enhanced spin Hall effect and spin-mixing conductance in a $Y_3Fe_5O_{12}$ /bcc- $W_{1-x}Cr_x$ heterostructure by bulk extrinsic scattering and interfacial electric field, *Phys. Rev. Appl.* **13**, 064043 (2020).
- [15] Q. Lu, Y. Li, B. Peng, H. Tang, Y. Zhang, Z. He, L. Wang, C. Li, W. Su, and Q. Yang, *et al.*, Enhancement of the spin-mixing conductance in Co-Fe-B/W bilayers by interface engineering, *Phys. Rev. Appl.* **12**, 064035 (2019).
- [16] S. Li, X. Zhao, W. Liu, Y. Song, L. Liu, X. Zhao, and Z. Zhang, Interface effect of ultrathin W layer on spin-orbit torque in Ta/W/CoFeB multilayers, *Appl. Phys. Lett.* **114**, 082402 (2019).
- [17] P. Yang, Q. Shao, G. Yu, C. He, K. Wong, X. Lu, J. Zhang, B. Liu, H. Meng, and L. He, *et al.*, Enhancement of the spin-orbit torque efficiency in W/Cu/CoFeB heterostructures via interface engineering, *Appl. Phys. Lett.* **117**, 082409 (2020).
- [18] S. Karube, N. Tezuka, M. Kohda, and J. Nitta, Anomalous spin-orbit field via the Rashba-Edelstein effect at the W/Pt interface, *Phys. Rev. Appl.* **13**, 024009 (2020).
- [19] G. Allen, S. Manipatruni, D. E. Nikonorov, M. Doczy, and I. A. Young, Experimental demonstration of the coexistence of spin Hall and Rashba effects in β -tantalum/ferromagnet bilayers, *Phys. Rev. B* **91**, 144412 (2015).
- [20] R. Hao, K. Zhang, W. Chen, J. Qu, S. Kang, X. Zhang, D. Zhu, and W. Zhao, Significant role of interfacial spin-orbit coupling in the spin-to-charge conversion in Pt/NiFe heterostructure, *ACS Appl. Mater. Interfaces* **14**, 57321 (2022).
- [21] L. Wang, R. Wesselink, Y. Liu, Z. Yuan, K. Xia, and P. J. Kelly, Giant room temperature interface spin Hall and inverse spin Hall effects, *Phys. Rev. Lett.* **116**, 196602 (2016).
- [22] N. Behera, S. Chaudhary, and D. K. Pandya, Anomalous anti-damping in sputtered β -Ta/Py bilayer system, *Sci. Rep.* **6**, 19488 (2016).
- [23] E. Pandey, P. Sharangi, A. Sahoo, S. P. Mahanta, S. Mallik, and S. Bedanta, A perspective on multifunctional ferromagnet/organic molecule spinterface, *Appl. Phys. Lett.* **123**, 040501 (2023).
- [24] S. Alotibi, B. J. Hickey, G. Teobaldi, M. Ali, J. Barker, E. Poli, D. D. O'Regan, Q. Ramasse, G. Burnell, and J. Patchett, *et al.*, Enhanced spin-orbit coupling in heavy metals via molecular coupling, *ACS Appl. Mater. Interfaces* **13**, 5228 (2021).
- [25] B. B. Singh, S. K. Jena, M. Samanta, K. Biswas, B. Satpati, and S. Bedanta, Inverse spin Hall effect in electron beam evaporated topological insulator Bi_2Se_3 thin film, *Phys. Status Solidi RRL* **13**, 1800492 (2019).
- [26] P. Gupta, B. B. Singh, K. Roy, A. Sarkar, M. Waschk, T. Brueckel, and S. Bedanta, Simultaneous observation of anti-damping and the inverse spin Hall effect in the $La_{0.67}Sr_{0.33}MnO_3/Pt$ bilayer system, *Nanoscale* **13**, 2714 (2021).
- [27] G. Kresse and J. Furthmüller, Efficient iterative schemes for *ab initio* total-energy calculations using a plane-wave basis set, *Phys. Rev. B* **54**, 11169 (1996).
- [28] G. Kresse and D. Joubert, From ultrasoft pseudopotentials to the projector augmented-wave method, *Phys. Rev. B* **59**, 1758 (1999).
- [29] J. P. Perdew, K. Burke, and M. Ernzerhof, Generalized gradient approximation made simple, *Phys. Rev. Lett.* **77**, 3865 (1996).
- [30] N. Behera, P. Guha, D. K. Pandya, and S. Chaudhary, Capping layer (Cl) induced antidamping in Cl/Py/ β -W system (Cl: Al, β -Ta, Cu, β -W), *ACS Appl. Mater. Interfaces* **9**, 31005 (2017).
- [31] See Supplemental Material at <http://link.aps.org/supplemental/10.1103/PhysRevApplied.21.054001> for additional structural analysis, magnetic characterization, DFT results, and angle-dependent ISHE measurements.
- [32] R. Meilunas, R. Chang, S. Liu, M. Jensen, and M. M. Kappes, Infrared and Raman spectra of C_{60} and C_{70} solid films at room temperature, *J. Appl. Phys.* **70**, 5128 (1991).
- [33] F. Cataldo, Raman spectra of C_{60} fullerene photopolymers prepared in solution, *Eur. Polym. J.* **36**, 653 (2000).
- [34] M. Belmeguenai, M. Gabor, F. Zighem, N. Challab, T. Petrisor, R. Mos, and C. Tiusan, Ferromagnetic-resonance-induced spin pumping in $Co_{20}Fe_{60}B_{20}/Pt$ systems: Damping investigation, *J. Phys. D: Appl. Phys.* **51**, 045002 (2018).
- [35] P. Sharangi, E. Pandey, S. Mohanty, S. Nayak, and S. Bedanta, Spinterface-induced modification in magnetic properties in $Co_{40}Fe_{40}B_{20}$ /fullerene bilayers, *J. Phys. Chem. C* **125**, 25350 (2021).
- [36] B. B. Singh and S. Bedanta, Large spin Hall angle and spin-mixing conductance in the highly resistive antiferromagnet Mn_2Au , *Phys. Rev. Appl.* **13**, 044020 (2020).
- [37] P. Sharangi, A. Mukhopadhyaya, S. Mallik, E. Pandey, B. Ojha, M. E. Ali, and S. Bedanta, Effect of fullerene on the anisotropy, domain size and relaxation of a perpendicularly magnetized Pt/Co/ C_{60} /Pt system, *J. Mater. Chem. C* **10**, 17236 (2022).
- [38] X. Shi, A. Pang, K. Man, R. Zhang, C. Minot, M. S. Altman, and M. A. Van Hove, C_{60} on the Pt(111) surface: Structural tuning of electronic properties, *Phys. Rev. B* **84**, 235406 (2011).
- [39] Q. Hao and G. Xiao, Giant spin Hall effect and switching induced by spin-transfer torque in a W/ $Co_{40}Fe_{40}B_{20}/MgO$ structure with perpendicular magnetic anisotropy, *Phys. Rev. Appl.* **3**, 034009 (2015).
- [40] A. Conca, B. Heinz, M. Schweizer, S. Keller, E. T. Papaioannou, and B. Hillebrands, Lack of correlation between the spin-mixing conductance and the inverse spin Hall effect generated voltages in CoFeB/Pt and CoFeB/Ta bilayers, *Phys. Rev. B* **95**, 174426 (2017).
- [41] K. Shanavas, Z. S. Popović, and S. Satpathy, Theoretical model for Rashba spin-orbit interaction in *d* electrons, *Phys. Rev. B* **90**, 165108 (2014).
- [42] V. Amin and M. Stiles, Spin transport at interfaces with spin-orbit coupling: Phenomenology, *Phys. Rev. B* **94**, 104420 (2016).
- [43] M. Zahedinejad, H. Fulara, R. Khymyn, A. Houshang, M. Dvornik, S. Fukami, S. Kanai, H. Ohno, and J. Åkerman, Memristive control of mutual spin Hall nano-oscillator synchronization for neuromorphic computing, *Nat. Mater.* **21**, 81 (2022).